Synergistic effects of silver nanoparticles and cisplatin in combating inflammation and hyperplasia of airway stents

Zhaonan Li [a,1], Chuan Tian [a,1], Dechao Jiao [a], Jing Li [a], Yahua Li [a], Xueliang Zhou [a], Huiping Zhao [b], Yanan Zhao [a,*], Xinwei Han [a,**]

[a] Department of Interventional Radiology, First Affiliated Hospital of Zhengzhou University, Zhengzhou, 450001, PR China
[b] Department of Radiology, First Affiliated Hospital of Zhengzhou University, Zhengzhou, 450001, PR China

ARTICLE INFO

ABSTRACT

Anti-inflammatory and antihyperplasia activities are essential requirements for the successful use of airway stents. In this work, silver nanoparticles (AgNPs) and cisplatin (DDP) were combined in a synergistic modification strategy to improve the surface function of airway stents. Using polycaprolactone (PCL) as a drug carrier, a dual-functional PCL-AgNPs-DDP fiber film-coated airway stent was fabricated by electrospinning. The physicochemical and biological properties of the obtained fiber films were examined. The ATR-FTIR, XPS, SEM-EDS and TEM results suggested that AgNPs and DDP could be successfully immobilized onto the airway stent surface. The drug release and surface degradation results revealed that AgNPs and DDP can undergo sustained release from films for 30 d, and the weight loss was approximately 50% after 35 d. In addition, the dual-functional fiber film suppressed human embryonic lung fibroblast growth and exhibited excellent antibacterial activity against *Staphylococcus aureus, Pseudomonas aeruginosa* and *Candida albicans*. Furthermore, the effectiveness of the dual-functional fiber film-coated airway stent was evaluated by application to the trachea of New Zealand rabbits. The *in vivo* results indicated that PCL-AgNPs-DDP fiber film-coated airway stent can significantly inhibit granulation tissue formation and collagen deposition, reduced the expression of IL-8, TNF-α, IL-1α, PCNA, α-SMA and CD68, and ultimately achieved anti-inflammatory and antihyperplasia effects. Hence, this study provides a dual-functional surface-coated airway stent to address the clinical complications associated with respiratory tract inflammation and granulation tissue hyperplasia, thus inhibiting tracheal stenosis.

1. Introduction

Tracheal stenosis (TS) is an obstruction of the airway resulting in shortness of breath and dyspnea [1]. Airway stent implantation is an effective method for the treatment of TS due to its minimal invasiveness, short recovery time and favorable recovery effect. Currently, a variety of commercial airway stents, such as nickel-titanium alloy stents, silicone stents and ^{125}I stents, have been designed to overcome the shortcomings of previously reported stents and have been gradually introduced into modern practice [2,3]. However, common complications related to airway stent implantation, including respiratory tract inflammation and granulation tissue hyperplasia, can easily cause tracheal restenosis, and therefore clinical needs are still not satisfied [4].

Stent-related respiratory tract inflammatory stimulation is the main cause of TS. On the one hand, after airway stent implantation, the tracheal wall in contact with the stent exhibits congestion, redness and swelling, and plasma exudate easily forms a membrane-like substance that adheres to the airway wall, resulting in the retention of sputum and infection. A prospective study revealed that the bacterial colonization rate of stents was as high as 78% in a short time (3–4 weeks) after stent implantation [5]. A meta-analysis of 501 patients with airway stents showed that 93 (19%) experienced stent-related respiratory tract

infection, and the incidence of infection varied with the type of stent [6]. Besides, Ost et al. further found that respiratory infections increase the risk of granulation tissue formation following airway stenting in patients with malignant TS [7]. On the other hand, inflammation promoters and inflammatory suppressors are activated/inhibited in a temporal manner and simultaneously recruit neutrophils, macrophages, and T cells to the inflammatory area to remove necrotic tissue and promote damage repair. However, when the above regulatory process is abnormal, inflammatory responses lead to high expression levels of basic fibroblast growth factor (bFGF), collagen and α-smooth muscle actin (α-SMA) and stimulate the proliferation and differentiation of fibroblasts and the deposition of a large amount of extracellular matrix, resulting in granulation tissue hyperplasia. Therefore, airway stents with dual anti-inflammatory and antihyperplasia properties may be highly effective in combatting TS.

With advances in nanotechnology, several metal nanomaterials have been applied in biomedical fields. Silver nanoparticles (AgNPs) have attracted widespread attention because of their strong bactericidal, anti-inflammatory and anti-cancer properties [8,9]. Due to the wide range of infectious diseases caused by different pathogens and to increasing antibiotic resistance, biomedical products containing AgNPs not only have effective antibacterial ability that avoids antibiotic resistance but also can improve inflammatory microenvironment [10–13]. However, some researchers are concerned about the toxicity and safety of AgNPs to humans during use. Actually, the toxicity of AgNPs can vary by more than 1-2 orders of magnitude depending on its size, shape, and size distribution, and silver accumulated in organs can mostly be cleared after 8 weeks [14]. An animal study using rats revealed that no adverse reactions were observed when taking silver nanoparticles orally. Another clinical study of patients taking commercial colloidal silver products found that all patients had no observable toxic effects [15]. In addition, several studies have shown that AgNPs coated on a polyurethane stent are effective in suppressing tracheal restenosis caused by bacterial adherence and subsequent bacterial biofilm (BBFs) formation [16–18]. Thus, it will be optimal to select AgNPs to reduce BBFs and inhibit TS.

Certain drugs, such as paclitaxel, gemcitabine, sorafenib, and cisplatin (DDP), can be used to endow stents with more effective anti-hyperplasia activity. These drugs usually block cell cycle progression by inhibiting DNA synthesis. Among them, DDP is the most effective anti-cancer drug and has been applied in the clinical treatment of esophageal cancer, breast cancer, ovarian cancer and lung cancer [19,20]. Recently, several studies have indicated that DDP can inhibit the proliferation of fibroblasts in different tissues. Xu et al. revealed that DDP has significant antiproliferative and antifibrotic effects on primary human vocalfold fibroblasts [21]. Moreover, in dermatological studies, DDP (1 mM) induced apoptosis of myofibroblasts *in vitro* by activating caspase-3, thereby reducing the growth of scars [22]. In summary, the combination of AgNPs and DDP may synergistically inhibit the formation of granulation tissue.

Herein, as shown in Fig. 1, we constructed a dual-functional airway stent with anti-inflammatory and antihyperplasia effects by electrospinning technology. The resultant PCL-DDP-AgNPs fiber film-coated airway stents were then implanted into the trachea of New Zealand rabbits. The synergistic effect of DDP and AgNPs release *in vivo* led to bacterial death, decreased levels of inflammatory factors (such as TNF-α, IL-1α, and IL-8), and decreased α-SMA and collagen deposition, thus preventing TS.

2. Materials and methods

2.1. Materials

Polycaprolactone (PCL, Mn = 100000 g/mol) was provided by Changchun SinoBiomaterials Co., Ltd. (Changchun, China). Silver nanoparticles (AgNPs, d = 15–20 nm) were obtained from Shanghai Yurui Chemical Co., Ltd. (Shanghai China). AgNPs is a black powder with a solid content of more than 25%, a particle size of 15–20 nm, a density of 2.07 g/cm³, and a purity of 99.99%. Cisplatin (DDP) was purchased from Sigma-Aldrich Trading Co., Ltd. (Shanghai, China). Both covered and uncovered self-expandable metallic stents (20 mm × 8 mm) were purchased from Micro-Tech Medical Technology Co., Ltd (Nanjing
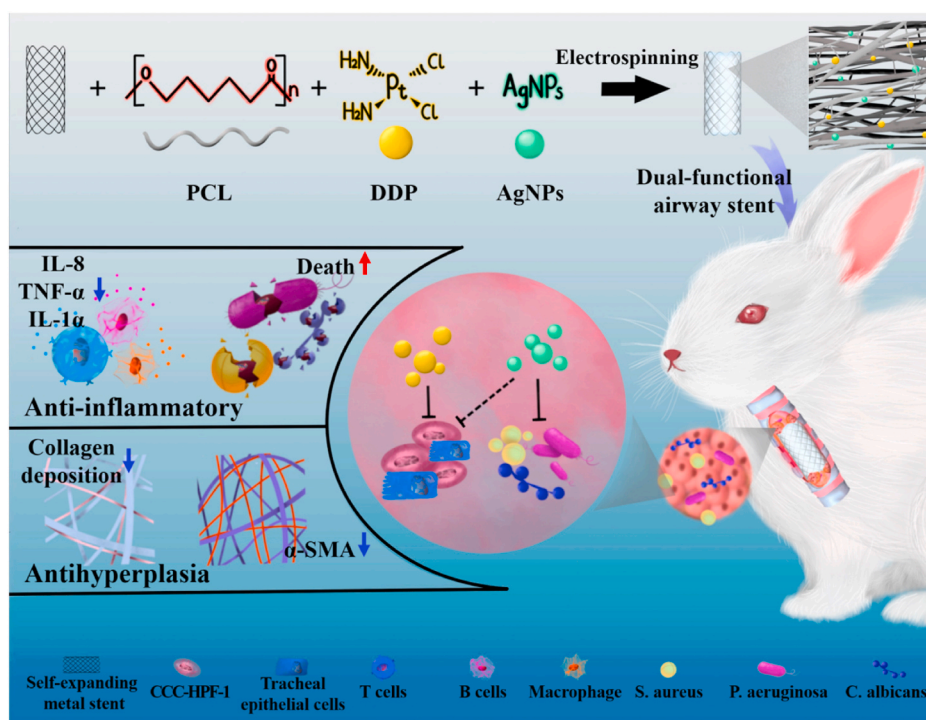

Fig. 1. Synergistic modification with silver nanoparticles and cisplatin formed the dual-functional PCL-DDP-AgNPs fiber-coated airway, which could significantly prevent trachea stenosis by reducing the inflammatory response and inhibiting granulation tissue hyperplasia.

China). Human embryonic lung fibroblast cells (CCC-HPF-1) were obtained from the Shanghai Cell Center (Chinese Academy of Sciences). Dulbecco's modified Eagle's medium (DMEM, D6429), fetal bovine serum (FBS, F8687), penicillin-streptomycin (V900929), and trypsin-EDTA (59417C) were supplied by Sigma-Aldrich Trading Co., Ltd. (Shanghai, China). Cell Counting Kit-8 (CCK-8, CK04) was obtained from Dojindo China Co., Ltd. (Shanghai, China). Rabbit ELISA kits for interleukin 8 (IL-8, SEA080Rb), tumor necrosis factor α (TNF-α, SEA133Rb) and interleukin 1α (IL-1α, SEA056Rb) were purchased from Wuhan USCN Business Co., Ltd. (Wuhan, China). The antibody against caspase-3 (abs119676) was purchased from Ibis Biotechnology Co., Ltd. (Shanghai China). Antibody CD68 (NBP2-48023) was purchased from Bio-techne China Co., Ltd. (Shanghai China). α-SMA (MAB1420) was purchased from Bio-Techne China Co., Ltd. (Shanghai, China). The LIVE/DEAD™ Viability/Cytotoxicity Kit (L3224), LIVE/DEAD™ BacLight™ Bacterial Viability Kit (L7012) and Annexin V-FITC Apoptosis Detection Kit (BMS500FI-100) were purchased from Thermo Fisher Scientific Co., Ltd. (China, Shanghai). Hexafluoroisopropanol (HFIP, 38701-74-5), ethanol (64-17-5), glutaraldehyde (111-30-8) and para-formaldehyde (30525-89-4) were obtained from Sinopharm Chemical Reagent Co., Ltd. (Shanghai, China). The alanine aminotransferase assay kit (ALT, C052), aspartate aminotransferase assay kit (AST, C072), total bilirubin assay kit (TBIL, C004), albumin assay kit (ALB, C008), urea nitrogen determination kit (BUN, C010), and creatinine determination kit (CR, C051) were purchased from Changchun Huili Biotechnology Co., Ltd. (Changchun, China).

2.2. Sample preparation

The electrospinning parameters and drug content of the fiber films were as recommended in previous reports [23–26]. In brief, 1.25 g of PCL was first dissolved in 10 mL of hexafluoroisopropanol (HFIP) to prepare the PCL solution. Then, 0.05 g of AgNPs was dissolved in the above solution to prepare the PCL-4%AgNPs solution. Similarly, PCL-4% DDP and PCL-4%DDP-4%AgNPs solutions were prepared as shown in Table 1. These solutions were electrospun at 15 kV using a high-voltage power supplier, a flow rate of 0.5 mL/h, and collectors positioned 20 cm from the needle tip. The self-expanding metal airway stent (SEMS) needed to be aligned with the roller collector to collect fiber films. The resultant fiber-coated airway stents were coded as PCL, PCL-AgNPs, PCL-DDP and PCL-DDP-AgNPs. All the obtained fiber films and fiber film-coated airway stents were used after being dried.

2.3. Surface characterization

The morphology of the PCL, PCL-AgNPs, PCL-DDP and PCL-DDP-AgNPs was analyzed by scanning electron microscopy (SEM) using a microscope (JSM-7401F, JEOL, Japan) equipped with an energy dispersive spectroscopy (EDS) analysis system. Before observation, the samples were mounted separately and vacuum-coated with gold–palladium for 60 s. Additionally, at least four images of each sample were obtained. The average diameter of the electrospun fibers was measured with Adobe Photoshop CS6 image analysis software (Adobe, California, USA) using at least 50 different randomly selected fibers from each image. The size and morphology of AgNPs in the fibers were observed by transmission electron microscopy (TEM, JEM-2100F, JEOL, Tokyo, Japan). The size distribution was determined by counting over

100 particles in representative TEM images. The chemical groups were investigated by attenuated total reflection infrared spectroscopy (ATR-FTIR, Nicolet 6700, Thermo Fisher Scientific). The surface chemical compositions were tested by X-ray photoelectron spectroscopy (XPS, XSAM600, UK). The hydrophilicity/hydrophobicity of the different fiber films was examined by water contact angle testing. In detail, the various fiber films were cut into pieces of approximately 1×1 cm^2, and deionized water was dropped on the sample surface. The contact angle was analyzed and recorded using a Krüss GmbH DSA 100 Mk 2 goniometer (Krüss GmbH, Hamburg, Germany).

2.4. Delivery of AgNPs and DDP

To evaluate the release behavior of the AgNPs fiber films, the films were first cut into small squares approximately 10 mg in weight and then immersed in 5 mL of PBS. The suspension was kept in a thermocontrolled water bath under shaking at 50 rpm and 37 °C. At predetermined time intervals, 1.0 mL of the release solution was collected for analysis, and 1.0 mL of fresh PBS was added to the extraction bottles. At various time points (0–25 d), the amount of released AgNPs was examined by graphite-furnace atomic absorption spectrometry (GF-AAS, Avanta M, GBC Scientific Equipment). Additionally, the amount of DDP released from the films was estimated three times over 0–25 d by UV–Vis spectroscopy (Hitachi UV–vis spectrophotometer) at 220 nm in the release medium (i.e., PBS, pH 7.4). The release behavior was calculated using standard curves constructed from serial concentrations of DDP.

2.5. Surface degradation

The degradation behavior of the fiber films *in vitro* was studied in PBS and tracheal simulation fluid (TSF). First, the films were cut into small squares with a total mass of 100 mg, which were then placed in 5 mL of PBS or 5 mL of TSF and incubated at 37 °C. The suspension was kept in a constant-temperature water bath under shaking at 80 cycles per minute. The buffer solution was replaced daily. At predetermined intervals, the samples were carefully withdrawn, rinsed three times with distilled water, dried and weighed. The weight loss of each film was calculated according to the following equation [27,28]:

$$Weight\ loss(\%) = \frac{W_o - W_t}{W_o} \times 100\%$$

where w_0 represents the initial weight of the dried film, and w_t represents the weight of the dried film after degradation at predetermined intervals.

2.6. Antibacterial evaluation in vitro

In this work, the bacterial species *Staphylococcus aureus* (ATCC 25923), *Pseudomonas aeruginosa* (ATCC 27853) and *Candida albicans* (ATCC 10231) were used to evaluate the antibacterial activity. These strains were revived and diluted to a suitable concentration for further use.

2.6.1. Bacterial proliferation assay
The fiber films were cut into 1×1 cm^2 pieces and then exposed to ultraviolet light for 30 min for sterilization. Afterwards, the samples were deposited in each well of a 6-well plate. Each sample was incubated in 2 mL of liquid medium and 20 μL of bacterial suspension at 37 °C for 24 h. At the specified time, 200 μL of bacterial suspension was transferred to sterile 96-well plates, and the absorbance at 595 nm was measured by a microplate reader (NanoDrop, Thermo Fisher, USA).

2.6.2. Colony formation assay
The obtained material was cut into 1×1 cm^2 samples, and each side was exposed to ultraviolet (UV) light for 30 min for sterilization. Then, a

Table 1
Sample codes and compositions of the fiber films.

Sample code	PCL (g)	AgNPs (g)	DDP (g)	HFIP (g)
PCL	1.25	0	0	15.96
PCL-AgNPs	1.25	0.05	0	15.96
PLA-DDP	1.25	0	0.05	15.96
PLA-DDP-AgNPs	1.25	0.05	0.05	15.96

fragment of the sterile material was deposited in a 6-well plate. Each material was incubated in 2 mL of liquid medium and 20 μL of microbial suspension at 37 °C for 24 h (*S. aureus*, *P. aeruginosa* and *C. albicans*). Moreover, the obtained bacterial solution was diluted with PBS within a concentration range of 10^{-3} to 10^{-7}, and 100 μL of bacterial solution was homogeneously seeded in dishes with Luria-Bertani (LB) medium. The antibacterial activity was calculated as the percentage of bacterial reduction using the following equation [29]:

$$Inhibition\ rate\ (\%) = \frac{Co - C}{Co} \times 100\%$$

where Co and C refer to the average colony number after incubation without and with samples, respectively.

2.6.3. Live/dead BacLight bacterial viability assay

The samples (1×1 cm^2) were added to a 12-well plate containing 3 mL of LB broth and 60 μL of bacterial suspension (adjusted to 5.0×10^9 CFU mL^{-1}) for overnight culture. After incubation for 72 h, each film was first washed three times with PBS and then stained with SYTO 9 dye (stains live cells, green) and propidium iodide (stains dead cells, red). Finally, the films were observed with a 63x air objective under a confocal laser scanning microscope (CLSM, Zeiss LSM 800, Germany). The images were analyzed by Image-Pro Plus software (Media Cybernetics, Silver Spring, MD, USA) and COMSTAT software for the bacterial biofilms (BBFs) [30–32].

2.7. Antihyperplasia property evaluation in vitro

To examine the antihyperplasia properties of PCL, PCL-AgNPs, PCL-DDP, and PCL-DDP-AgNPs fiber films, human embryonic lung fibroblast cells (CCC-HPF-1) were selected as the model cells.

2.7.1. CCK-8 assay

The proliferation of CCC-HPF-1 cells was measured by CCK-8 assay. In short, the fiber films were incubated in cell culture medium, and the supernatant was collected on days 1, 2, and 3. Then, the cells (3×10^4/mL) were incubated with the extracts in a 96-well plate (200 μL/well) at 37 °C in 5% CO$_2$. After incubation, 100 μL of fresh culture medium and 10 μL of CCK-8 reagent were added and further incubated for another 2 h for color development. The optical density (OD) at 450 nm was determined with a microplate reader (NanoDrop, Thermo Fisher, USA).

2.7.2. Live/dead cell staining assay

Live/dead staining assays were performed using a live/dead viability kit. In brief, CCC-HPF-1 cells (4×10^4/mL) were cultured on fiber films for 1 d and 2 d. Then, 5 μL of 4 mM calcein-AM (component A) and 20 μL of mM ethidium homodimer-1 (component B) were diluted in 10 mL of PBS to obtain a staining solution. After removal of the cell culture medium, the cells were washed three times with PBS and stained with 200 μL of staining solution. After 20 min of incubation at 25 °C in the dark, the cells were imaged under a fluorescence microscope (Carl Zeiss, Germany). The total number of CCC-HPF-1 cells was analyzed by Image-Pro Plus software (Media Cybernetics, Silver Spring, MD, USA).

2.7.3. Apoptosis assay

CCC-HPF-1 cells were seeded in 6-well plates at a density of 1×10^5 cells/well. Then, the fiber films were incubated in the cell culture medium, and the supernatant was collected on days 1 and 2. After cell attachment, the different supernatants were added to the cells in 6-well plates. All samples were incubated for 24 h at 37 °C in a humidified atmosphere with 5% CO$_2$. Then, the rate of apoptosis was measured using an Annexin V-FITC Apoptosis Detection Kit in compliance with the manufacturer's protocol. Finally, cell apoptosis was assessed by flow cytometry (Cytoflex, Beckman, China).

2.8. Animal experiment

All implantation procedures were approved by the animal care committee of the First Affiliated Hospital of Zhengzhou University and following the National Institute of Health's guide for the care and use of laboratory animals (Ethics approval number: 2021-19) [33]. Thirty male New Zealand rabbits were obtained from the laboratory animal center of Hualan Biological Co., Ltd. (Henan, China). All New Zealand rabbits were randomly divided into four groups: the commercial airway stent group (control group), PCL-AgNPs-coated airway stent group, PCL-DDP-coated airway stent group, and PCL-DDP-AgNPs-coated airway stent group.

2.8.1. In vivo stent implantation

Before the procedure, the New Zealand rabbits were anesthetized via intramuscular injection. The animals were placed in a supine position with the neck hyperextended under fluoroscopic guidance (Artis zee DSA system, SIEMENS, Germany). The whole process was completed through a 5-Fr stent delivery system. A 12-Fr dilator (12-F dilator, Cook Medical) was used to dilate the entrance. Then, an intratracheal channel was created with a 0.035-inch guidewire (Terumo Corporation, Tokyo, Japan) and 5-Fr catheter (Terumo Corporation, Tokyo, Japan). The delivery system was pushed with the stent over the guidewire, and the stent was released at least 1.5–2 cm cranially to the carina (as shown in Fig. 6a). The animals were then clinically monitored and sacrificed 4 weeks after stenting.

2.8.2. Computed tomography

At 4 weeks after stenting, computed tomography scans (CT, Sensation 64, Siemens Medical Solutions, Germany) of the neck and chest were performed on New Zealand rabbits. In this study, 1-mm-thick slices with 0.5-mm intervals were used, and multiplanar reconstruction was performed.

2.8.3. Blood testing

At 1 and 4 weeks, 2 mL of blood was extracted from ear veins of rabbits and placed in anticoagulant tubes. The above samples were centrifuged at 4 °C 3000 rpm for 15 min to obtain the supernatant. The measurement type of ALT and AST is the rate method, TBIL and ALB is the end point method, and BUN and CR is the two-point rate method. Finally, all the above liver indexes and renal function indexes were detected on an automatic biochemical analyzer (Rayto, China).

2.8.4. Analysis of bacterial content in coated stents

The rabbits were sacrificed to test the effect of fiber film-coated airway stents on biofilm production in the trachea. At 4 weeks, the fiber films were peeled from the different stents. The obtained films were placed in a sterile tube and washed with sterile saline (SSW) 3 times to remove nonadherent microorganisms. The tested films with 1 mL SSW were sonicated for 30 s to collect the bacteria from the films. The obtained bacterial suspension was diluted and inoculated onto solid medium plates to quantify the number of viable bacteria. Finally, the bacterial content in the trachea was compared between different groups, and linear regression was used to analyze the relationship between the bacterial content in the trachea and the growth of granulation tissue.

Additionally, the rabbit lungs were washed twice with 25 mL of sterilized PBS from the lower part of the tracheal stent to obtain bronchoalveolar lavage fluid (BALF). BALF was centrifuged at 4 °C to obtain the supernatant. The level of IL-8, TNF-α and IL-1α in the supernatant was detected by ELISA kits. The microtiter plate was pre-coated with an antibody specific to IL-8. Then, the supernatant or standards was added to the microtiter plate wells with a biotin-conjugated antibody specific to IL-8. Next, Avidin conjugated to Horseradish Peroxidase (HRP) was added to each microplate well. After TMB substrate solution was added, only the wells containing IL-8 change color as a result of the reaction between biotin-conjugated antibody and enzyme-conjugated Avidin.

The enzyme-substrate reaction was terminated by the addition of sulphuric acid solution. Finally, the absorbance at 450 nm was measured by a microplate reader (NanoDrop, Thermo Fisher, USA). The concentration of IL-8 in the supernatant was determined by comparing the OD value of the samples to the standard curve. The level of TNF-α and IL-1α were detected by steps of IL-8 mentioned above.

2.8.5. Histopathological evaluation

At 4 weeks after implantation, the rabbits were sacrificed by inhalation of pure carbon dioxide. Subsequently, tracheal specimens were obtained by transverse incision near the proximal and distal ends of the airway stent. After being embedded in paraffin, the tracheal specimens were cut into sections and analyzed by hematoxylin and eosin (H&E) staining and Masson's trichrome (MT) staining. The granulation tissue thickness was analyzed by ImageJ software. The degree of inflammation and the degree of collagen deposition were measured by H&E and MT according to a previous study [18,34,35]. In addition, histological sections of tracheal specimens were separately stained with
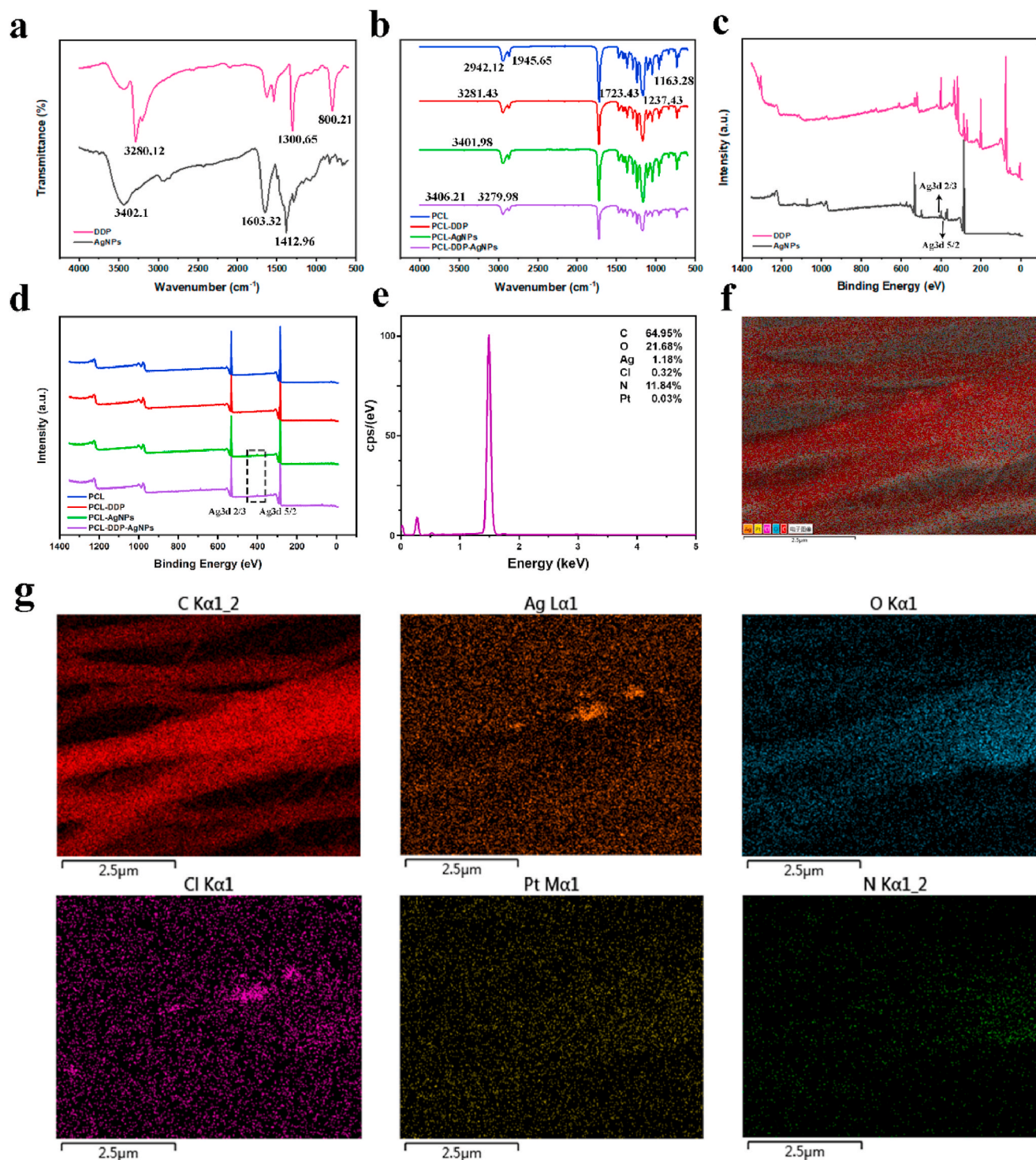

Fig. 2. FTIR (a–b) and XPS (c–d) spectra of AgNPs powder, DDP powder, PCL fiber film, PCL-AgNPs fiber film, PCL-DDP fiber film and PCL-DDP-AgNPs fiber film, respectively. EDS spectrum (e) and elemental mapping (f, g) of PCL-DDP-AgNPs fiber films. Scale bar, 2.5 μm.

antibodies against Caspase-3, PCNA, α-smooth muscle actin (α-SMA), and CD68. The expression levels of collagen deposition, caspase-3, PCNA, α-SMA and CD68 were determined by Image-Pro Plus software (Media Cybernetics, Silver Spring, MD, USA). Heart, liver, spleen, lung and kidney samples were collected and tested by H&E staining.

2.9. Statistical analyses

The results are presented as the mean ± S.D. for all independent experiments. The data were examined by two-way ANOVA or Student's *t*-test, as appropriate, using GraphPad Prism 7.0 software, and statistically significant values are indicated by $*p < 0.05$, $**p < 0.005$, $***p < 0.0005$.

3. Results and discussions

3.1. Characterization of dual-functional surface coating

To load AgNPs and DDP, PCL was used as the drug carrier to fabricate a dual-functional surface coating on the SEMS by electrospinning. The chemical structure and composition of the PCL, PCL-AgNPs, PCL-DDP and PCL-DDP-AgNPs fiber films were examined by ATR-FTIR and XPS. As shown in Fig. 2a, the DDP spectrum exhibited strong absorption peaks at 3280.76 cm^{-1}, 1300.21 cm^{-1}, and 800.43 cm^{-1}, corresponding to -N-H- stretching vibration absorption [36,37]. The FTIR spectrum of AgNPs exhibited prominent peaks at 3402.1 cm^{-1}, 1,603.32 cm^{-1}, and 1412.96 cm^{-1}. In Fig. 2b, the intense peak at 1723.43 cm^{-1} is assigned to the stretching mode of carbonyl groups of PCL. The peaks at 2942.12 cm^{-1} correspond to the asymmetric stretching of CH2 groups in the PCL polymer backbone. The C–O–C stretching vibration spectrum in PCL was clearly shown at 1237.43 cm^{-1} and 1163.28 cm^{-1} [38]. The FTIR spectrum of PCL-AgNPs fiber films exhibited the characteristic peaks of PCL and AgNPs, indicating the introduction of AgNPs into the fiber films. Similarly, DDP was successfully introduced into the PCL-DDP fiber films, and AgNPs and DDP were both present in the PCL-DDP-AgNPs fiber films, which was also confirmed by XPS analysis in Fig. 2c-d [39–41]. As shown in Fig. 2e–g, the EDS elemental maps of PCL-DDP-AgNPs fiber films showed C, Ag, O, Cl, Pt, and N, respectively. The results further indicated the existence of AgNPs and DDP.

Then, SEM was used to examine the morphology of the prepared fiber films. As shown in Fig. 3a, all films exhibited randomly interconnected structures and the fibers are uniform in size. Obviously, AgNPs and DDP crystals were observed on the surface of the fibers, indicating the deposition of AgNPs and DDP crystals on the fiber. The average diameters of the PCL, PCL-AgNPs, PCL-DDP and PCL-DDP-AgNPs fibers were 276.2 ± 111.8, 243.7 ± 99.8, 233.3 ± 107.6, and 298.8 ± 101.1 nm, respectively (Fig. 3b). Additionally, AgNPs in the PCL-AgNP nanofiber films were further tested by TEM. The TEM images showed that the AgNPs had a spherical shape, which is consistent with the previous literature [42]. It is known that the antibacterial activity of AgNPs is influenced by their size and that small AgNPs have stronger antibacterial properties. In Fig. 3e–f, the dimensions of AgNPs calculated from the TEM images are 15–20 nm, indicating that the AgNPs used in this work have excellent antibacterial properties (as shown in Fig. 4). To clarify the influence of AgNPs and DDP on the surface properties of the fiber films, the water contact angle was measured. For PCL, PCL-AgNPs, PCL-DDP and PCL-DDP-AgNPs, the water contact angles were 123.9 ± 3.1°, 132.1 ± 4.5°, 111.8 ± 2.9° and 124.4 ± 3.7°, respectively (Fig. 3c–d). The water contact angle of the film was greater than 100°, which indicated that they were hydrophobic and beneficial to prevent sputum adhesion and improve airway cleanliness.

3.2. Drug release and degradation in vitro

The drug release behavior of PCL, PCL-AgNPs, PCL-DDP and PCL-DDP-AgNPs was studied in PBS (pH 7.4). As shown in Fig. 3g–h, the

DDP and AgNPs release behavior of PCL-DDP, PCL-AgNPs and PCL-DDP-AgNPs could be described by two phases: the burst-release phase and constant-release phase. In detail, the burst release of DDP from PCL-DDP and PCL-DDP-AgNPs in the first eight days was 71.7 ± 3.1% and 76.7 ± 2.9%, respectively. The release of AgNPs from PCL-AgNPs and PCL-DDP-AgNPs in the first eight days was 50.6 ± 2.8% and 51.7 ± 1.7%, respectively. Although there was a sudden release from the drug-loaded fibrous film, the trachea was a closed environment with no flowing liquid. Under normal circumstances, the drug would continue to be present on the surface of the trachea.

Additionally, *in vitro* degradation studies were carried out to analyze the biodegradation of the PCL, PCL-AgNPs, PCL-DDP, and PCL-DDP-AgNPs fiber films. Specifically, PBS (pH = 7.4) and TSF were used to complete the degradation study over 35 d. As shown in Fig. 3i–j, the degradation rate of PCL-DDP-AgNPs in PBS and TSF was faster than those of PCL, PCL-AgNPs, and PCL-DDP ($p < 0.05$). This result may be related to the degradation process of AgNPs and the rapid release of DDP. Moreover, compared with the degradation process in PBS, the degradation rate of PCL, PCL-AgNPs, PCL-DDP and PCL-DDP-AgNPs were much faster in TSF ($p < 0.05$). To the best of our knowledge, the presence of enzymes in the tracheal solution and the relatively weak acidity may be associated with this result. During the observation period, the weight loss of PCL, PCL-AgNPs, PCL-DDP and PCL-DDP-AgNPs in PBS was 55.2 ± 1.1%, 65.1 ± 1.3%, 59.7 ± 2.9% and 70.0 ± 1.8%, respectively, and the corresponding weight loss in TSF was 58.8 ± 2.1%, 69.0 ± 3.0%, 62.7 ± 3.0% and 73.8 ± 2.3%, respectively. The degradation results showed that with the addition of DDP and AgNPs to the PCL material, the degradation time of the fiber films tended to be shortened. However, since the observation time of this study was 1 month, the degradation trend of the material was in line with the published literature on this subject.

3.3. Antibacterial evaluation in vitro

BBFs are membrane-like products formed by the accumulation and encapsulation of their clones by the secretion of alginate poly glyco-protein complexes after the pathogen adheres to the surface of airway stents or pathological tissues [43–45]. The BBF formation the surface of the airway stent after implantation will lead to prolonged infection, which could promote stent restenosis. Therefore, constructing an *in situ* antibacterial airway stent is essential for inhibiting infection.

In this work, AgNPs were selected to endow airway stents with antibacterial performance against common airway bacteria, such as *S. aureus, P. aeruginosa,* and *C. albicans.* As shown in Fig. 4a, the PCL fiber film with AgNPs could specifically bind with bacterial oxidation-reducing enzyme Q or react with bacterial nucleic acid and protein to form an irreversible combination to inhibit bacterial proliferation and diffusion.

The antibacterial performance of the fiber films was fully evaluated. As shown in Fig. 4b, the bacterial proliferation results confirmed that the PCL-AgNPs and PCL-DDP-AgNPs films containing AgNPs markedly inhibited *S. aureus, P. aeruginosa,* and *C. albicans* growth within 24 h, in contrast to the PCL and PCL-DDP films. The inhibition rates were calculated and are shown in Fig. 4c. The inhibition rates after 24 h of PCL, PCL-AgNPs, PCL-DDP, and PCL-DDP-AgNPs were −1.23%, 85.23%, 1.34% and 82.34%, respectively. The results of the Live/Dead Baclight Bacterial Viability Assay was determined by COMSTAT software analysis. As shown in Fig. 4d, the main image showed the merge image of living and dead bacteria in each group, and the thickness of bacterial biofilm was shown in the right and bottom images. In the PCL group, the majority of the *S. aureus, P. aeruginosa* and *C. albicans* were stained in green, and the intensity of green fluorescence was the strongest. With the addition of DDP or AgNPs, the green fluorescence intensity representing the living bacteria decreased gradually, while the red fluorescence intensity representing the dead bacteria increased gradually. Compare with the other three groups, the PCL-DDP-AgNPs
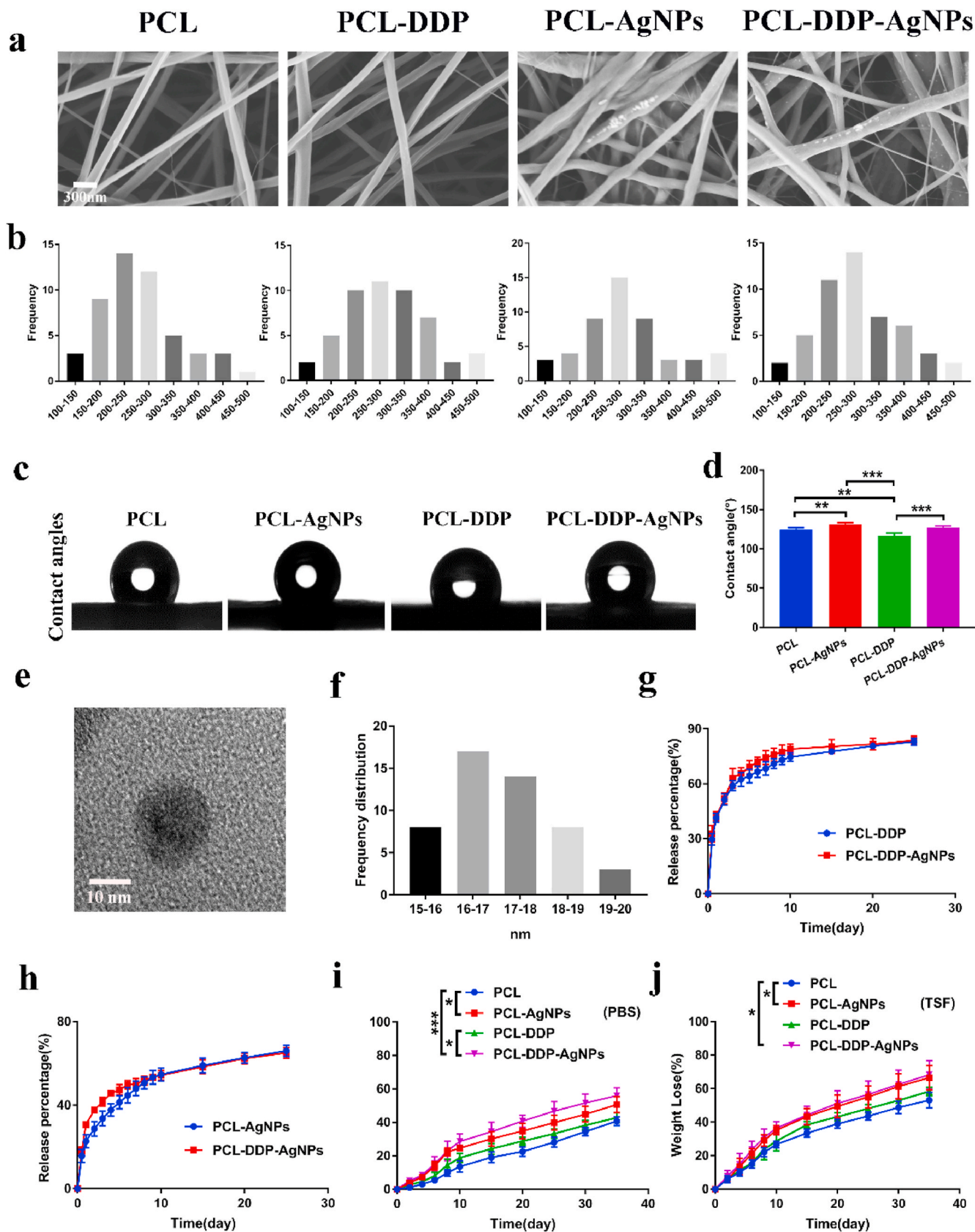
Fig. 3. SEM images (a) and fiber diameter distribution (b) of PCL, PCL-DDP, PCL-AgNPs and PCL-DDP-AgNPs fiber films, respectively. Representative images (c) and statistical analyze (d) of the water contact angle. TEM image of AgNPs (e). Size distribution of AgNPs in fiber films calculated from TEM images (f). Drug release of DDP and AgNPs from different drug-loaded fiber films (g, h). Degradation behaviors of PCL, PCL-DDP, PCL-AgNPs and PCL-DDP-AgNPs in PBS (pH 7.4) or tracheal simulated fluid (TSF) (i, j). *p < 0.05, **p < 0.005, ***p < 0.0005. Scale bar, 10 nm and 200 nm.
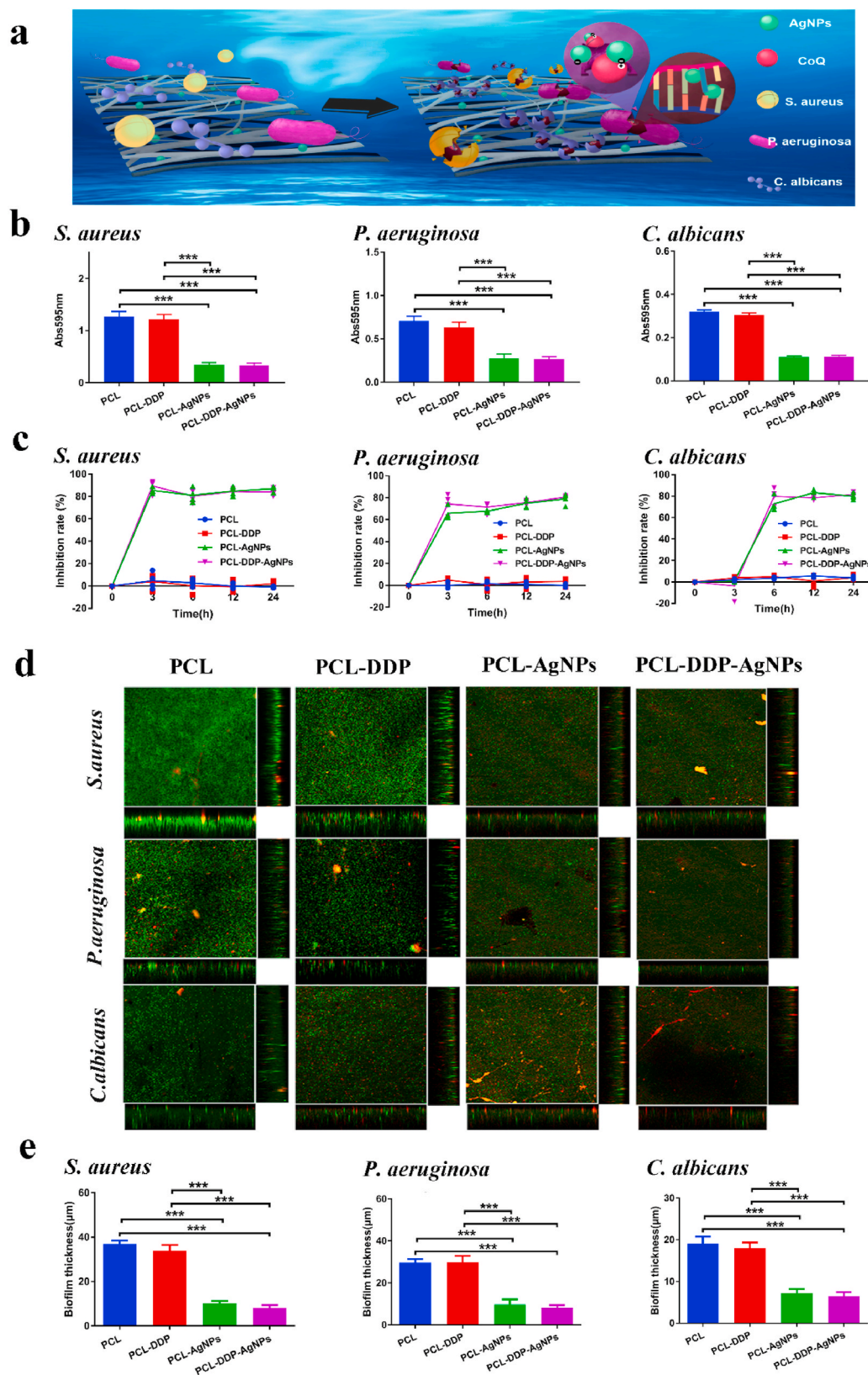
Fig. 4. Schematic illustration of the antibacterial mechanism of AgNPs (a). The absorbance values (b) and inhibition ratio (c) for PCL, PCL-DDP, PCL-AgNPs and PCL-DDP-AgNPs incubated with *Staphylococcus aureus, Pseudomonas aeruginosa* and *Candida albicans* cultures for 24 h, respectively. CLSM images (sum of stack images and orthogonal views) after staining with the Live/Dead BacLight Bacterial Viability Kit (d). COMSTAT2 was used to analyze the biofilm thickness of *Staphylococcus aureus, Pseudomonas aeruginosa* and *Candida albicans* on different fiber films (e). *p < 0.05, **p < 0.005, ***p < 0.0005.

group showed lowest green fluorescence intensity and highest red fluorescence intensity. The quantitative statistical results in Fig. 4e further indicated that the PCL-AgNPs and PCL-DDP-AgNPs films could significantly reduce the biofilm thickness, which is helpful to decrease the infection after airway stent implantation. In conclusion, the PCL-AgNPs and PCL-DDP-AgNPs films exhibited obvious advantages in terms of inhibiting the aggregation and growth of bacteria and could act as a suitable airway stent coating to repair TS.

3.4. Antihyperplasia evaluation in vitro

In addition to the antibacterial ability, the effect of functional surfaces on human embryonic lung fibroblast (CCC-HPF-1) inhibition is also important. CCC-HPF-1 cells were derived from 15-week embryonic tissues that were induced to labor and were sourced from the Institute of Basic Medicine, Chinese Academy of Medical Sciences. The cells belong

to the same cell line as human airway fibroblasts, so inflammation expression and tissue structure are similar, especially in granulation tissue formation. Thus, in this section, we evaluated the growth behaviors of CCC-HPF-1 on PCL, PCL-AgNPs, PCL-DDP, and PCL-DDP-AgNPs release buffers.

As shown in Fig. 5a, we inoculated CCC-HPF-1 cells directly onto the different fiber films for 1 d and 2 d of culture and performed live/dead
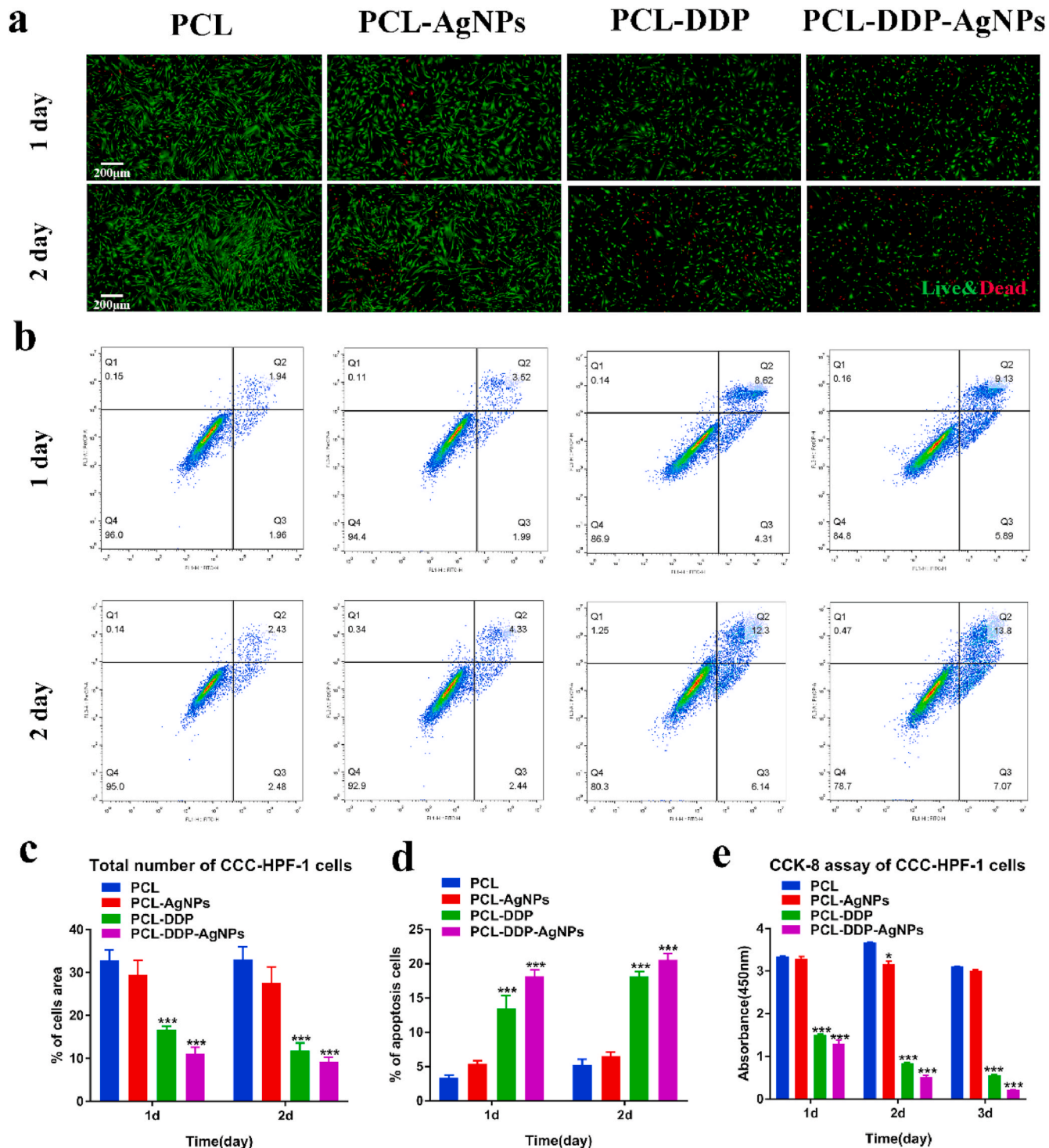

Fig. 5. The Live/dead staining assays of CCC-HPF-1 cells cultured on PCL, PCL-DDP, PCL-AgNPs and PCL-DDP-AgNPs for 1 d and 2 d, respectively (a). The apoptotic effect of AgNPs and DDP released from PCL-AgNP, PCL-DDP and PCL-DDP-AgNP films for 1 d and 2 d against CCC-HPF-1 cells, respectively (b). Statistical analysis of live CCC-HPF-1 cells on different films (c). Statistical analysis of apoptotic cells on different films (d). CCK-8 assay of CCC-HPF-1 cells at 1, 2, and 3 days, respectively (e). *p < 0.05, **p < 0.005, ***p < 0.0005. Scale bar, 200 μm.

staining analysis to evaluate the inhibition of cells transplanted onto the scaffolds. Fluorescence microscopy showed that the live cells (green) were the least abundant on the PCL-DDP-AgNPs film, followed by the PCL-DDP film, while the PCL and PCL-AgNPs films showed no significant difference in the proliferation of CCC-HPF-1. In Fig. 5c, we quantitatively analyzed the number of cells on the film surface and found that the number of cells was significantly lower on the PCL-DDP and PCL-DDP-AgNPs films than on the PCL and PCL-AgNPs films.

Furthermore, the proliferation of CCC-HPF-1 cells was analyzed with a CCK-8 assay. Fig. 5e shows that the OD value of the PCL group was similar to that of the PCL-AgNPs, indicating that the AgNPs showed favorable biocompatibility with CCC-HPF-1 cells. In contrast, the OD was significantly reduced in the PCL-DDP and PCL-DDP-AgNPs groups, suggesting that the DDP released in the buffer inhibited the proliferation of CCC-HPF-1. Consequently, the incubation of CCC-HPF-1 with the release buffer for 1, 2, and 3 d showed a clear time-dependent pattern, which indicated that with prolonged DDP release, the activity of CCC-HPF-1 cells was significantly inhibited.

To examine the apoptosis of CCC-HPF-1 cells cultured in release buffer (release concentration from 1 d to 2 d), apoptosis was performed using an apoptosis staining kit (Fig. 5b and d). The results illustrated that the number of apoptotic cells was similar in the PCL and PCL-AgNPs release buffers. These data further confirm that the PCL-AgNPs film has favorable compatibility. In the PCL-DDP and PCL-DDP-AgNPs release buffers, the number of apoptotic cells was significantly higher, which is consistent with the results of the CCK-8 assay, indicating that DDP can directly induce CCC-HPF-1 apoptosis. As a result, this finding preliminarily indicated that the PCL-DDP and PCL-DDP-AgNPs surfaces possess better antihyperplasia properties.

3.5. In vivo airway stent implantation

The above experiments confirmed that the dual-functional surface was antibacterial and anti-hyperplastic. First, AgNPs can positively regulate the surface microenvironment to inhibit tracheal bacterial growth. Second, the *in situ* DDP-releasing property reduces granulation tissue hyperplasia. To further verify the potential of this dual-functional surface-coated airway stent for reducing inflammation and preventing tracheal stenosis, *in vivo* airway stent implantation was performed.

3.5.1. Correlation analysis between inflammation and granulation tissue formation

Fig. 6a displays the process of airway stent implantation under the guidance of DSA. The results in Fig. 6b show that the operative time in the control, PCL-AgNPs, PCL-DDP, and PCL-DDP-AgNPs groups was similar, indicating that there was no difference in the influence on the respiration and cardiopulmonary function of rabbits in the different groups.

At 4 weeks after implantation, the tracheal anatomy and airway stents in the four groups were examined by curved planar reconstruction (CPR) and the volume rendering technique (VRT), respectively. As shown in Fig. 6c, obvious granulation tissue formation (red square) was observed in the control group, while the least granulation tissue was formed in the contact between the PCL-DDP-AgNPs airway stent end and the trachea. Observing the positional relationship between the stent and the tissue by VRT showed that the four groups of stents did not shift or fall off in the airway. Moreover, the fitting degree of the airway stent and trachea in the PCL-DDP-AgNPs group was the best in comparison to the other three groups.

The lung condition results are shown in Fig. 6d. In the control group and PCL-DDP group, a large number of inflammatory cells proliferated, and some alveolar structures were damaged, which indicated that the release of DDP in the trachea could achieve a certain degree of anti-hyperplasia effect, but due to the lack of AgNPs to inhibit the bacterial population in the airway, the protective function of normal lung tissue was reduced. This result indicated that, compared with the airway stent

loaded with arsenic trioxide in our previous work, the PCL-DDP-AgNPs airway stent not only inhibited the hyperplasia of granulation tissue but also had an anti-inflammatory effect endowed by the addition of AgNPs. Therefore, the rational use of antibacterial materials or drugs in the development of functional airway stents is necessary to improve tracheal or lung inflammation in patients.

To clarify the potential anti-inflammatory mechanism of reducing lower respiratory tract infection after implantation, we studied the expression of IL-8, IL-1α and TNF-α in rabbit BALF. IL-8, TNF-α and IL-1α are systemic inflammatory cytokines, which can promote the chemotaxis of inflammatory cells and induce the proliferation of fibroblasts [46–48]. Previous studies have indicated that IL-8, TNF-α and IL-1α have favorable sensitivity, specificity and accuracy in stent-related studies, which can detect early systemic and pulmonary inflammatory responses and may predict the development of stent-induced TS [49,50]. As shown in Fig. 6e–g, the levels of IL-8, TNF-α and IL-1α in the AgNP-containing groups (PCL-AgNPs and PCL-DDP-AgNPs) were remarkably decreased compared with those in the groups without AgNPs (control and PCL-DDP). Therefore, the results indicated better control over inflammation in the PCL-DDP-AgNPs group, which is in line with the clinical expectations of airway stents in terms of inhibiting inflammation.

The general observation of the trachea in different groups is displayed in Fig. 6h. In the control group, the trachea was swollen and showed severe adhesion to surrounding tissue, whereas there was no adherence to surrounding tissues in the PCL-DDP-AgNPs group. Then, the trachea was cut open to remove the airway stent. The surface coating from the airway stent was stripped and incubated on the LB culture to examine the bacterial content. As shown in Fig. 6i, the bacterial content in AgNP-containing groups was also markably decreased in contrast with those in non-AgNP-containing groups. In Fig. 6j, the correlation between the bacterial content on the surface coating and the thickness of granulation tissue showed that the use of stents containing AgNPs could inhibit bacterial growth and reduce the formation of tracheal granulation tissue after stenting. These results are consistent with previous results and confirm that reducing the inflammatory reaction can inhibit granulation tissue hyperplasia [51,52].

3.5.2. Dual-functional PCL-DDP-AgNPs airway stent inhibits tracheal stenosis

The tracheal specimens obtained from the proximal or distal ends of the airway stent were harvested. To investigate the antihyperplasia properties, H&E staining was first performed to observe granulation tissue thickness. As clearly shown in the H&E images (Fig. 7a), the control group exhibited the thickest granulation tissue, whereas the dual-functional PCL-DDP-AgNPs group showed significantly reduced granulation tissue. The statistical analysis in Fig. 7b revealed that the granulation tissue thickness was markedly reduced in the PCL-DDP-AgNPs group (438.25 ± 37.67 μm) compared to that in the control group (910.75 ± 100.27 μm). Immunofluorescence staining of caspase-3 and PCNA was further performed. As shown in Fig. 7d–e, the control group had a low caspase-3-positive area (4.2 ± 0.75%) and a high PCNA-positive area (15.2 ± 1.33%). In contrast with the control, the dual-functional PCL-DDP-AgNPs airway stent significantly improved the caspase-3-positive area (17.8 ± 0.75%) and reduced the PCNA-positive area (2.60 ± 0.49%). Moreover, MT staining and immunohistochemical staining of α-SMA were performed. Collagen is the main component of the extracellular matrix, and excessive collagen deposition can gradually form scarring and cause restenosis of the trachea [53]. The MT images showed that the degree of collagen deposition was 4.25 ± 0.43% for the control group, 3.13 ± 0.59% for the PCL-AgNPs group, 2.88 ± 0.78% for the PCL-DDP group, and 2.25 ± 0.43% for the PCL-DDP-AgNPs group (Fig. 7c), indicating that the dual-functional PCL-DDP-AgNPs airway stent could exceedingly inhibit collagen deposition. α-SMA is a signature indicator of myofibroblasts, and the upregulation of α-SMA results in tracheal restenosis [54,55]. The α-SMA analysis (Fig. 7f) showed that the α-SMA-positive area in the PCL-DDP-AgNPs group (4.40 ± 1.12%) was
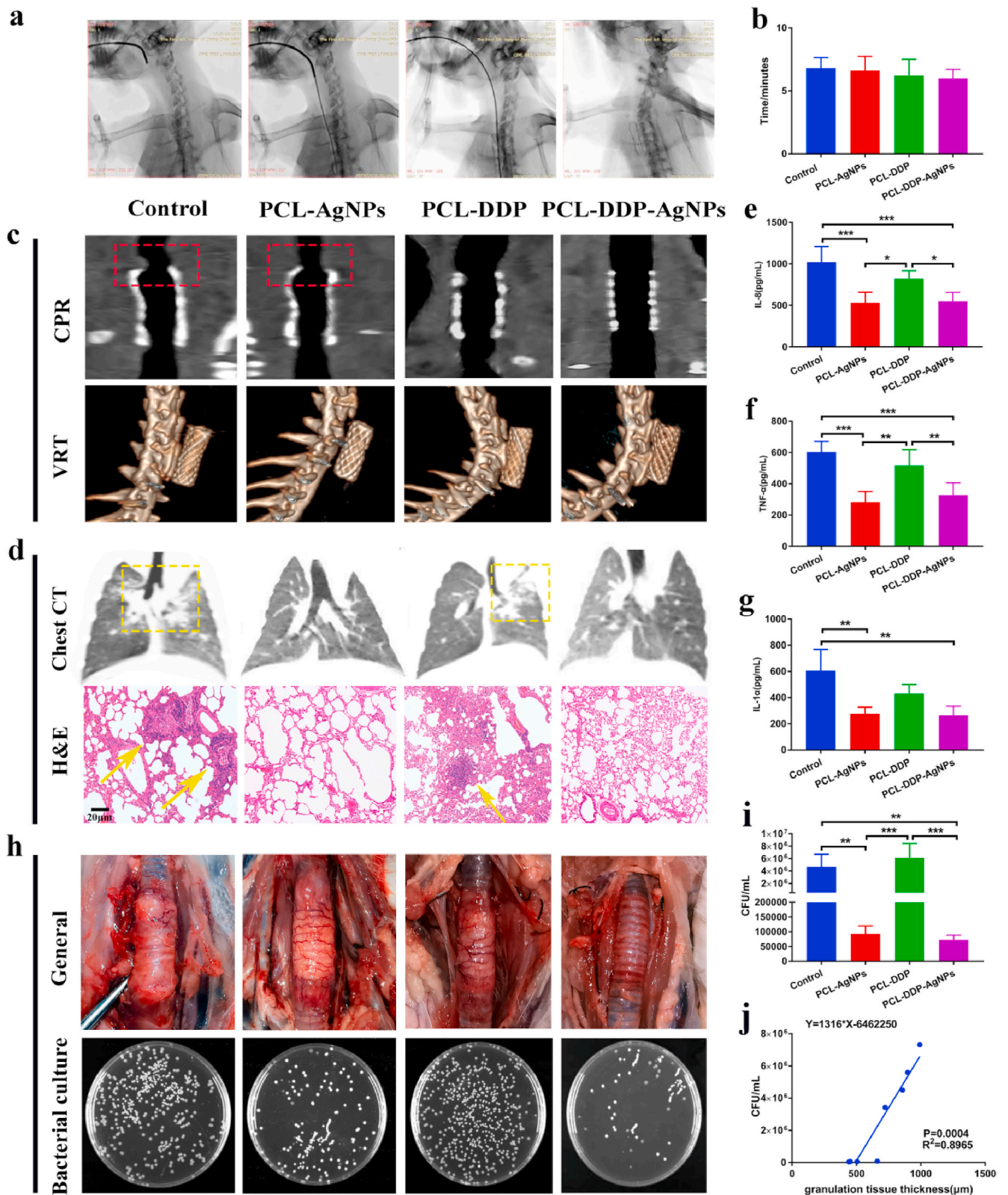
Fig. 6. Diagrams of the process of airway stent implantation in the trachea of New Zealand rabbits under DSA fluoroscopic monitoring (a). Statistical results of operation time for the control, PCL-DDP, PCL-AgNPs and PCL-DDP-AgNPs groups (b). The relationship between the stents and tracheal tissue was demonstrated by the curved planar reconstruction (CPR) technique at 4 weeks after stenting. The whole stent of different groups in the trachea was displayed by the volume rendering technique (VRT) (c). Chest CT and H&E staining of the lungs in different groups (d). Expression levels of IL-8, TNF-α and IL-1α in rabbit's BALF (e–g). General observation of the rabbit trachea in different groups. Graphical representation of the bacterial content on the surface of the different films (CFU/mL) (h). Statistical analysis of bacterial content on different films (i). Correlation analysis of bacterial content and granulation tissue formation between the control group and PCL-AgNPs group (j). *p < 0.05, **p < 0.005, ***p < 0.0005.
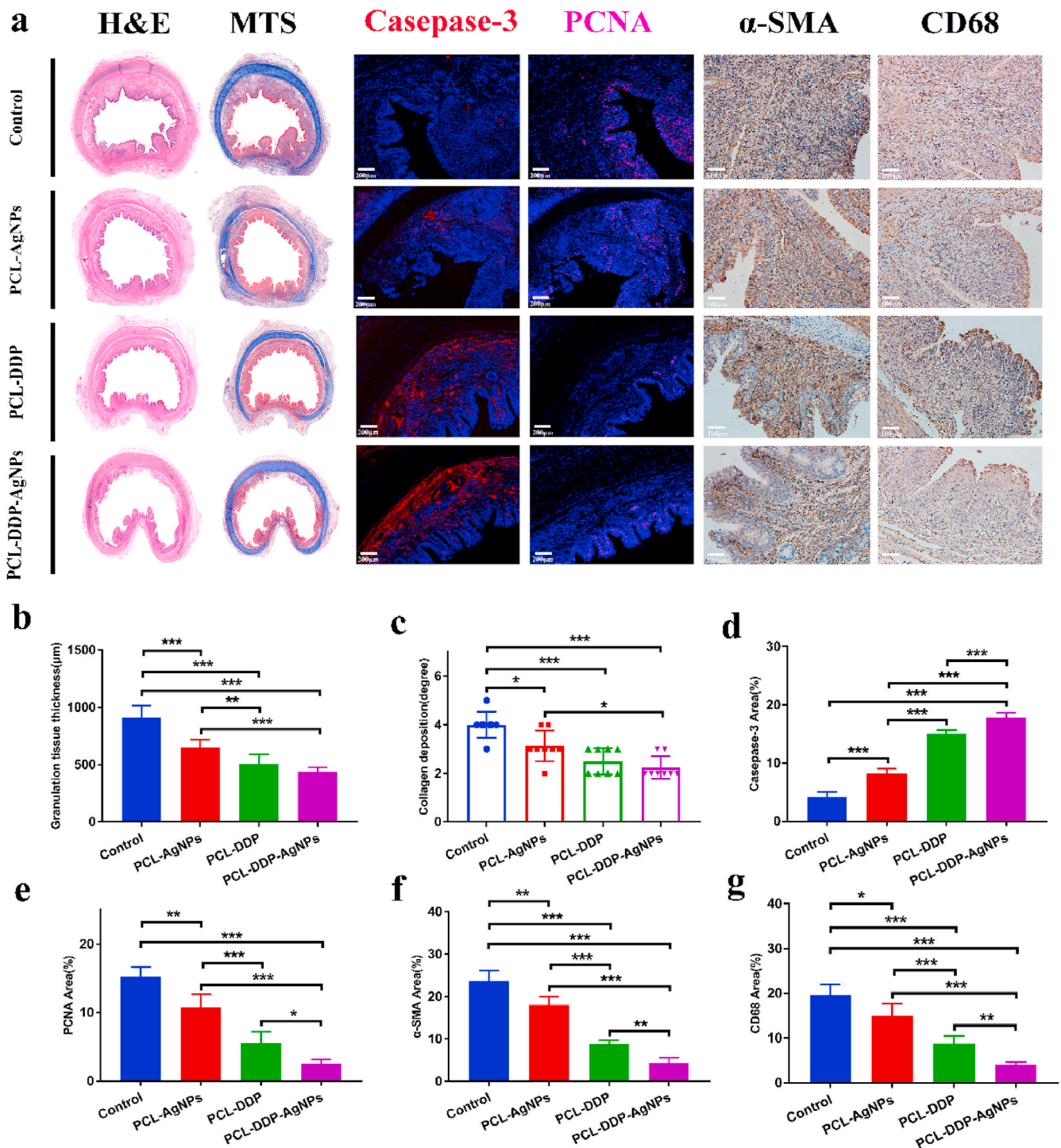
Fig. 7. H&E staining, MTS, Casepase-3, PCNA, α-SMA and CD68 of the tracheal samples in the control, PCL-DDP, PCL-AgNPs and PCL-DDP-AgNPs fiber film-coated airway stent (a). Statistical analysis of granulation tissue thickness, collagen deposition, Casepase-3 area, PCNA area, α-SMA area and CD68 area (b–g). The degree of collagen deposition was determined subjectively, where 1 represents mild, 2 represents mild to moderate, 3 represents moderate, 4 represents moderate to severe, and 5 represents severe. *p < 0.05, **p < 0.005, ***p < 0.0005. Scale bar, 100 μm and 200 μm.

reduced compared to that in the control (23.6 ± 2.24%), PCL-AgNPs (18.0 ± 1.79%) and PCL-DDP (8.80 ± 0.75%) groups, indicating that the dual-functional PCL-DDP-AgNPs airway stent could suppress the expression of α-SMA. To further clearly investigate the anti-inflammatory effects, immunohistochemical staining of CD68 was also performed. As shown in Fig. 7g, compared to the control group (19.16 ± 2.17%), PCL-AgNPs group (15.87 ± 3.35%) and PCL-DDP group (9.17 ± 2.01%), the PCL-DDP-AgNPs group (3.06 ± 1.74%)

showed depressed expression of CD 68 at 4 weeks after implantation.

These above results confirmed that the dual-functional surface with AgNPs and DDP could significantly inhibit cell proliferation, collagen deposition, α-SMA expression, and the inflammatory response. The anti-inflammatory and antihyperplasia mechanisms of the PCL-DDP-AgNPs airway stent may be as follows: (1) AgNPs can specifically bind with bacterial oxidation-reducing enzyme Q or react with bacterial nucleic acid and protein to inhibit bacterial proliferation and diffusion [56]. (2)

AgNPs can trigger cell apoptosis by upregulating caspase-3 and Bax, and downregulating Bcl-2 in cells [57]. (3) DDP can impede cellular processes, such as replication and transcription [58]. Therefore, the dual-functional coating showed the synergistic effect of AgNPs and DDP, thus providing a microenvironment for significantly reducing tracheal stenosis *in vivo*.

Additionally, the safety of airway stents is an important indicator to evaluate their potential clinical application. As shown in Fig. 8a, the heart, liver, spleen, and kidneys in the different groups displayed no pathological changes. Moreover, the results in Fig. 8b–g indicated that
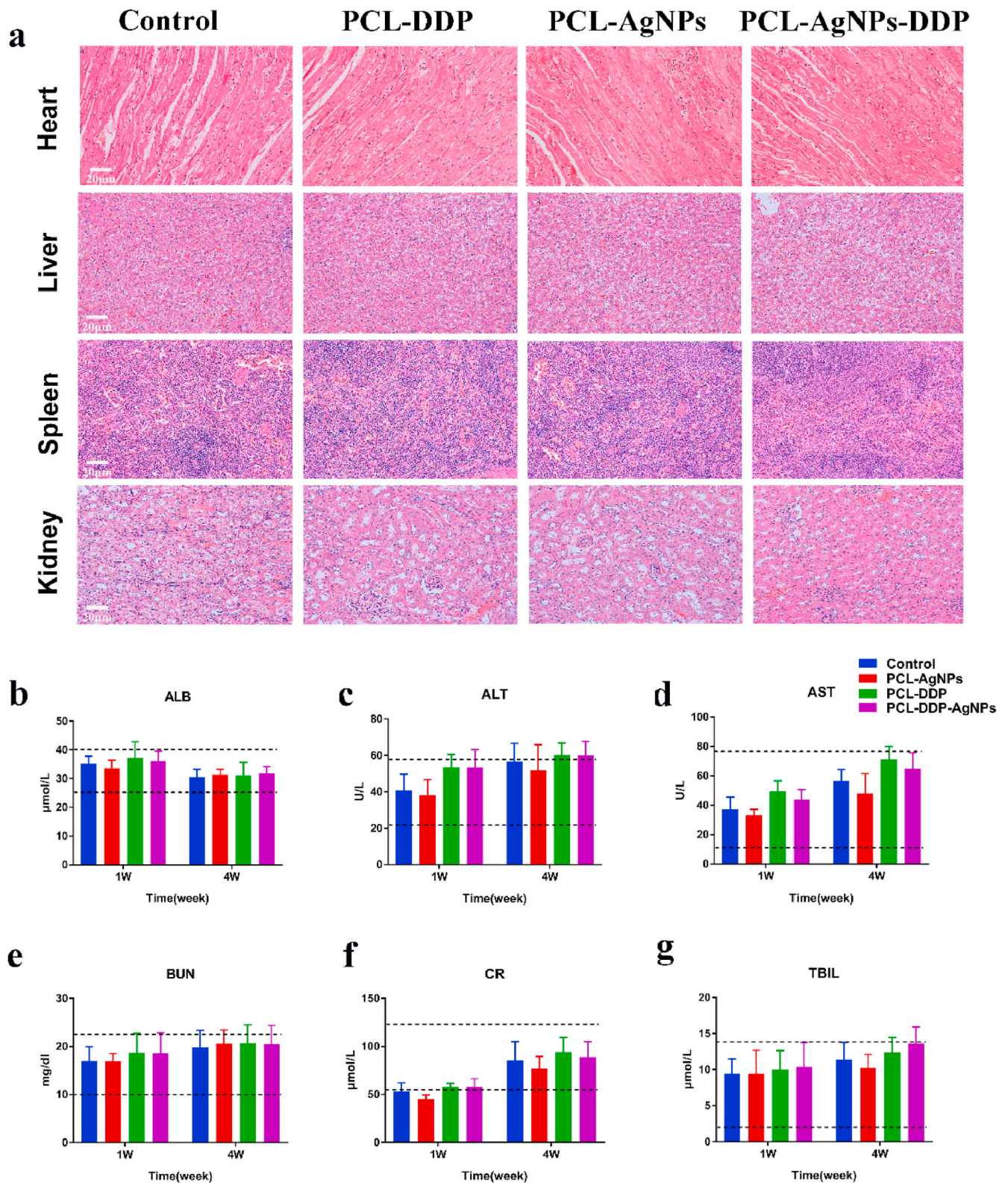

Fig. 8. H&E staining of the heart, liver, spleen, and kidney in the control, PCL-DDP, PCL-AgNPs and PCL-DDP-AgNPs fiber film-coated airway stents (a). The blood levels of ALB, ALT, AST, BUN, CR and TBIL in different groups of rabbits after 1 week and 4 weeks of stenting (b–g). Scale bar, 20 μm.

the liver and kidney functions remained within the normal range in different groups. The results confirmed that the dual-functional PCL-DDP-AgNPs airway stent is safe *in vivo*.

4. Conclusions

In this study, a series of fiber film-coated airway stents, including PCL-AgNPs, PCL-DDP and PCL-DDP-AgNPs, were successfully manufactured by electrospinning. The airway stents loaded with AgNPs/DDP showed sustained and controlled drug release and degradation kinetics. Specifically, AgNPs-containing airway stents showed favorable antibacterial properties and biocompatibility toward the trachea, while DDP-loaded stents could significantly inhibit human embryonic lung fibroblast growth. The *in vivo* experiments further confirmed that the synergy of AgNPs and DDP functions at the interface of the stent led to bacterial content reduction, inflammatory response reduction (3.06 ± 1.74%), collagen deposition (2.25 ± 0.43%) and α-SMA inhibition (4.40 ± 1.12%). In summary, this study provides a dual-functional surface with anti-inflammatory and antihyperplasia properties for airway stents, which would contribute to the improvement of clinical outcomes.

Data availability

All experimental data to support the findings from this study will be made available to interested investigators.

CRediT authorship contribution statement

Zhaonan Li: Writing – original draft, Methodology, Conceptualization, Writing – review & editing. **Chuan Tian:** Writing – original draft, Methodology, Software. **Dechao Jiao:** Formal analysis, Validation, Software. **Jing Li:** Formal analysis, Validation, Software. **Yahua Li:** Validation, Visualization. **Xueliang Zhou:** Validation, Visualization. **Huiping Zhao:** Resources, Data curation. **Yanan Zhao:** Supervision, Writing – review & editing, Funding acquisition. **Xinwei Han:** Supervision, Writing – review & editing, Funding acquisition.

Declaration of competing interest

The authors declare that they have no known competing financial interests or personal relationships that could have appeared to influence the work reported in this paper.

References

[1] D.F. Chen, Y. Chen, C.H. Zhong, X.B. Chen, S.Y. Li, Long-term efficacy and safety of the Dumon stent for benign tracheal stenosis: a meta-analysis, J. Thorac. Dis. 13 (1) (2021) 82–91.

[2] H. Dutau, A.I. Musani, S. Laroumagne, K. Darwiche, L. Freitag, P. Astoul, Biodegradable airway stents - bench to bedside: a comprehensive review, Respiration 90 (6) (2015) 512–521.

[3] W. Huang, Q. Shan, Z. Wu, H. Li, M. Zhou, X. Ding, et al., Retrievable covered metallic segmented Y airway stent for gastrorespiratory fistula of carina or main bronchi, J. Thorac. Cardiovasc. Surg. 161 (5) (2021) 1664–1671, 03-19.

[4] J. Ha, A. Mondal, Z. Zhao, A.K. Kaza, P.E. Dupont, Pediatric airway stent designed to facilitate mucus transport and atraumatic removal, IEEE Trans. Biomed. Eng. 67 (1) (2020) 177–184.

[5] M. Noppen, D. Pierard, M. Meysman, I. Claes, W. Vincken, Bacterial colonization of central airways after stenting, Am. J. Respir. Crit. Care Med. 160 (2) (1999) 672–677.

[6] M. Agrafiotis, Siempos II, M.E. Falagas, Infections related to airway stenting: a systematic review, Respiration 78 (1) (2009) 69–74.

[7] D.E. Ost, A.M. Shah, X. Lei, M. Godoy, C.A. Jimenez, G.A. Eapen, et al., Respiratory infections increase the risk of granulation tissue formation following airway stenting in patients with malignant airway obstruction, Chest 141 (6) (2012) 1473–1481.

[8] P. Mathur, S. Jha, S. Ramteke, N.K. Jain, Pharmaceutical aspects of silver nanoparticles, Artif. Cells Nanomed. Biotechnol. 46 (sup1) (2018) 115–126.

[9] S. Tang, J. Zheng, Antibacterial activity of silver nanoparticles: structural effects, Adv. Healthc. Mater. 7 (13) (2018), e1701503.

[10] A. Cochis, B. Azzimonti, V.C. Della, E. De Giglio, N. Bloise, L. Visai, et al., The effect of silver or gallium doped titanium against the multidrug resistant Acinetobacter baumannii, Biomaterials 80 (2016) 80–95.

[11] J. Wang, J. Li, S. Qian, G. Guo, Q. Wang, J. Tang, et al., Antibacterial surface design of titanium-based biomaterials for enhanced bacteria-killing and cell-assisting functions against periprosthetic joint infection, ACS Appl. Mater. Interfaces 8 (17) (2016) 11162–11178.

[12] I.X. Yin, J. Zhang, I.S. Zhao, M.L. Mei, Q. Li, C.H. Chu, The antibacterial mechanism of silver nanoparticles and its application in dentistry, Int. J. Nanomed. 15 (2020) 2555–2562.

[13] M. Poirier, J.C. Simard, F. Antoine, D. Girard, Interaction between silver nanoparticles of 20 nm (AgNP20) and human neutrophils: induction of apoptosis and inhibition of de novo protein synthesis by AgNP20 aggregates, J. Appl. Toxicol. 34 (4) (2014) 404–412.

[14] I.X. Yin, O.Y. Yu, I.S. Zhao, M.L. Mei, Q.L. Li, J. Tang, et al., Developing biocompatible silver nanoparticles using epigallocatechin gallate for dental use, Arch. Oral Biol. 102 (2019) 106–112.

[15] C. Liao, Y. Li, S.C. Tjong, Bactericidal and cytotoxic properties of silver nanoparticles, Int. J. Mol. Sci. 20 (2) (2019).

[16] F. Yang, Z. Ren, Q. Chai, G. Cui, L. Jiang, H. Chen, et al., A novel biliary stent coated with silver nanoparticles prolongs the unobstructed period and survival via anti-bacterial activity, Sci. Rep. 6 (2016) 21714.

[17] W. Wen, L.M. Ma, W. He, X.W. Tang, Y. Zhang, X. Wang, et al., Silver-nanoparticle-coated biliary stent inhibits bacterial adhesion in bacterial cholangitis in swine, Hepatobiliary Pancreat. Dis. Int. 15 (1) (2016) 87–92.

[18] W. Park, K.Y. Kim, J.M. Kang, D.S. Ryu, D.H. Kim, H.Y. Song, et al., Metallic stent mesh coated with silver nanoparticles suppresses stent-induced tissue hyperplasia and biliary sludge in the rabbit extrahepatic bile duct, Pharmaceutics 12 (6) (2020).

[19] M.C. Garassino, S. Gadgeel, E. Esteban, E. Felip, G. Speranza, M. Domine, et al., Patient-reported outcomes following pembrolizumab or placebo plus pemetrexed and platinum in patients with previously untreated, metastatic, non-squamous non-small-cell lung cancer (KEYNOTE-189): a multicentre, double-blind, randomised, placebo-controlled, phase 3 trial, Lancet Oncol. 21 (3) (2020) 387–397.

[20] W.Z. Zhong, Q. Wang, W.M. Mao, S.T. Xu, L. Wu, Y.C. Wei, et al., Gefitinib versus vinorelbine plus cisplatin as adjuvant treatment for stage II-IIIA (N1-N2) EGFR-mutant NSCLC: final overall survival analysis of CTONG1104 phase III trial, J. Clin. Oncol. (2020), JCO2001820.

[21] H. Xu, Q. Wang, G.K. Fan, The antiproliferative and antifibrotic effects of cisplatin on primary human vocal fold fibroblasts, ORL J. Otorhinolaryngol. Relat. Spec. 82 (4) (2020) 188–200.

[22] A. Nakazono-Kusaba, F. Takahashi-Yanaga, S. Morimoto, T. Sasaguri, Staurosporine-induced cleavage of alpha-smooth muscle actin during myofibroblast apoptosis, J. Invest. Dermatol. 119 (5) (2002) 1008–1013.

[23] Y.K. Chao, K.S. Liu, Y.C. Wang, Y.L. Huang, S.J. Liu, Biodegradable cisplatin-eluting tracheal stent for malignant airway obstruction: in vivo and in vitro studies, Chest 144 (1) (2013) 193–199.

[24] Y. Li, M. Li, X. Wang, Y. Wang, C. Li, Y. Zhao, et al., Arsenic trioxide-eluting electrospun nanofiber-covered self-expandable metallic stent reduces granulation tissue hyperplasia in rabbit trachea, Biomed. Mater. 16 (1) (2020) 15013.

[25] C. Mu, Q. Wu, Electrospun poly(epsilon-caprolactone) composite nanofibers with controlled release of cis-diamminediiodoplatinum for a higher anticancer activity, Nanoscale Res. Lett. 12 (1) (2017) 318.

[26] M. Maillard, F. Le Louedec, F. Thomas, E. Chatelut, Diversity of dose-individualization and therapeutic drug monitoring practices of platinum compounds: a review, Expet Opin. Drug Metabol. 16 (10) (2020) 907–925.

[27] M. Babjuk, M. Burger, R. Zigeuner, S.F. Shariat, B.W. van Rhijn, E. Comperat, et al., EAU guidelines on non-muscle-invasive urothelial carcinoma of the bladder: update 2013, Eur. Urol. 64 (4) (2013) 639–653.

[28] J. Wang, G. Wang, H. Shan, X. Wang, C. Wang, X. Zhuang, et al., Gradiently degraded electrospun polyester scaffolds with cytostatic for urothelial carcinoma therapy, Biomater. Sci. 7 (3) (2019) 963–974.

[29] A.G. Fane, R. Wang, M.X. Hu, Synthetic membranes for water purification: status and future, Angew Chem. Int. Ed. Engl. 54 (11) (2015) 3368–3386.

[30] J. Wu, F. Li, X. Hu, J. Lu, X. Sun, J. Gao, et al., Responsive assembly of silver nanoclusters with a biofilm locally amplified bactericidal effect to enhance treatments against multi-drug-resistant bacterial infections, ACS Cent. Sci. 5 (8) (2019) 1366–1376.

[31] N. Blanco-Cabra, K. Vega-Granados, L. Moya-Anderico, M. Vukomanovic, A. Parra, D.C.L. Alvarez, et al., Novel oleanolic and maslinic acid derivatives as a promising treatment against bacterial biofilm in nosocomial infections: an in vitro and in vivo study, ACS Infect. Dis. 5 (9) (2019) 1581–1589.

[32] A.A. Jack, H.R. Nordli, L.C. Powell, D. Farnell, B. Pukstad, P.D. Rye, et al., Cellulose nanofibril formulations incorporating a low-molecular-weight Alginate oligosaccharide modify bacterial biofilm development, Biomacromolecules 20 (8) (2019) 2953–2961.

[33] N.R.C.U. Care, A.U.O.L. Animals, Guide for the Care and Use of Laboratory Animals, National Academies Press (US), Washington (DC), 2011.

[34] J.H. Park, W. Park, S. Cho, K.Y. Kim, J. Tsauo, S.H. Yoon, et al., Nanofunctionalized stent-mediated local heat treatment for the suppression of stent-induced tissue hyperplasia, ACS Appl. Mater. Interfaces 10 (35) (2018) 29357–29366.

[35] E.J. Jun, J.H. Park, J. Tsauo, S.G. Yang, D.K. Kim, K.Y. Kim, et al., EW-7197, an activin-like kinase 5 inhibitor, suppresses granulation tissue after stent placement in rat esophagus, Gastrointest. Endosc. 86 (1) (2017) 219–228.

[36] K. Al-Jorani, A. Ruther, M. Martin, R. Haputhanthri, G.B. Deacon, H.L. Li, et al., The application of ATR-FTIR spectroscopy and the reversible DNA conformation as a sensor to test the effectiveness of platinum(II) anticancer drugs, Sensors 18 (12) (2018).

[37] K. Al-Jorani, A. Ruther, R. Haputhanthri, G.B. Deacon, H.L. Li, C. Cullinane, et al., ATR-FTIR spectroscopy shows changes in ovarian cancer cells after incubation with novel organoamidoplatinum(ii) complexes, Analyst 143 (24) (2018) 6087–6094.

[38] S. Radhakrishnan, S. Nagarajan, H. Belaid, C. Farha, I. Iatsunskyi, E. Coy, et al., Fabrication of 3D printed antimicrobial polycaprolactone scaffolds for tissue engineering applications, Mater. Sci. Eng. C Mater. Biol. Appl. 118 (2021) 111525.

[39] S. Guo, L. Miao, Y. Wang, L. Huang, Unmodified drug used as a material to construct nanoparticles: delivery of cisplatin for enhanced anti-cancer therapy, J. Contr. Release 174 (2014) 137–142.

[40] W.M. Girma, S.H. Tzing, P.J. Tseng, C.C. Huang, Y.C. Ling, J.Y. Chang, Synthesis of cisplatin(IV) prodrug-tethered CuFeS2 nanoparticles in tumor-targeted chemotherapy and photothermal therapy, ACS Appl. Mater. Interfaces 10 (5) (2018) 4590–4602.

[41] A.K. Thompson, C. Hackett, T.L. Grady, S. Enyinnia, Q.R. Moore, F.M. Nave, Development and characterization of membranes with PVA containing silver particles: a study of the addition and stability, Polymers 12 (9) (2020).

[42] C.Y. Chen, H. Yin, X. Chen, T.H. Chen, H.M. Liu, S.S. Rao, et al., Angstrom-scale silver particle-embedded carbomer gel promotes wound healing by inhibiting bacterial colonization and inflammation, Sci. Adv. 6 (43) (2020).

[43] L.K. Vestby, T. Gronseth, R. Simm, L.L. Nesse, Bacterial biofilm and its role in the pathogenesis of disease, Antibiotics (Basel) 9 (2) (2020).

[44] F. Schmal, W. Fegeler, H.J. Terpe, W. Hermann, W. Stoll, K. Becker, Bacteria and granulation tissue associated with Montgomery T-tubes, Laryngoscope 113 (8) (2003) 1394–1400.

[45] S.A. Nouraei, M.A. Petrou, P.S. Randhawa, A. Singh, D.J. Howard, G.S. Sandhu, Bacterial colonization of airway stents: a promoter of granulation tissue formation following laryngotracheal reconstruction, Arch. Otolaryngol. Head Neck Surg. 132 (10) (2006) 1086–1090.

[46] D. Morris, M. Ansar, J. Speshock, T. Ivanciuc, Y. Qu, A. Casola, et al., Antiviral and immunomodulatory activity of silver nanoparticles in experimental RSV infection, Viruses 11 (8) (2019).

[47] S. Periasamy, J.A. Harton, Interleukin 1alpha (IL-1alpha) promotes pathogenic immature myeloid cells and IL-1beta favors protective mature myeloid cells during acute lung infection, J. Infect. Dis. 217 (9) (2018) 1481–1490.

[48] S.A. Papiris, I.P. Tomos, A. Karakatsani, A. Spathis, I. Korbila, A. Analitis, et al., High levels of IL-6 and IL-8 characterize early-on idiopathic pulmonary fibrosis acute exacerbations, Cytokine 102 (2018) 168–172.

[49] P. Wei, Z. Huang, L. Gan, Y. Li, C. Qin, G. Liu, Nintedanib ameliorates tracheal stenosis by activating HDAC2 and suppressing IL-8 and VEGF in rabbit, Am. J. Transl. Res. 12 (8) (2020) 4739–4748.

[50] E. Arellano-Orden, C. Serrano, A. Montes-Worboys, V. Sanchez-Lopez, A. Laborda, F. Lostale, et al., Stent-induced tracheal stenosis can be predicted by IL-8 expression in rabbits, Eur. J. Clin. Invest. 47 (1) (2017) 84–92.

[51] P. Simoni, B.J. Wiatrak, Microbiology of stents in laryngotracheal reconstruction, Laryngoscope 114 (2) (2004) 364–367.

[52] C.T. Sasaki, M. Horiuchi, N. Koss, Tracheostomy-related subglottic stenosis: bacteriologic pathogenesis, Laryngoscope 89 (6 Pt 1) (1979) 857–865.

[53] Y. She, Z. Fan, L. Wang, Y. Li, W. Sun, H. Tang, et al., 3D printed biomimetic PCL scaffold as framework interspersed with collagen for long segment tracheal replacement, Front. Cell. Dev. Biol. 9 (2021) 629796.

[54] J.R. Olmos-Zuniga, M. Baltazares-Lipp, C. Hernandez-Jimenez, R. Jasso-Victoria, M. Gaxiola-Gaxiola, M. Silva-Martinez, et al., Treatment with hyaluronic acid and collagen-polyvinylpyrrolidone improves extracellular matrix assembly for scarring after tracheal resection, BioMed Res. Int. 2020 (2020) 3964518.

[55] H.J. Ahn, R. Khalmuratova, S.A. Park, E.J. Chung, H.W. Shin, S.K. Kwon, Serial analysis of tracheal restenosis after 3D-printed scaffold implantation: recruited inflammatory cells and associated tissue changes, Tissue Eng. Regen. Med. 14 (5) (2017) 631–639.

[56] J. Annamalai, N. Vasudevan, Enhanced biodegradation of an endocrine disrupting micro-pollutant: di (2-ethylhexyl) phthalate using biogenic self-assembled monolayer of silver nanoparticles, Sci. Total Environ. 719 (2020) 137115.

[57] X. Chang, X. Wang, J. Li, M. Shang, J. Niu, W. Zhang, et al., Silver nanoparticles induced cytotoxicity in HT22 cells through autophagy and apoptosis via PI3K/AKT/mTOR signaling pathway, Ecotoxicol. Environ. Saf. 208 (2021) 111696.

[58] L. Kelland, The resurgence of platinum-based cancer chemotherapy, Nat. Rev. Canc. 7 (8) (2007) 573–584.